CFD Simulation of Gas–Liquid Stirred Vessel: VC, S33, and L33 Flow Regimes

Avinash R. Khopkar and Vivek V. Ranade
Industrial Flow Modelling Group, National Chemical Laboratory, Pune 411 008, India

DOI 10.1002/aic.10762
Published online January 10, 2006 in Wiley InterScience (www.interscience.wiley.com).

A comprehensive computational model based on the Eulerian–Eulerian approach was developed to simulate gas–liquid flows in a stirred vessel. A separate submodel was developed to quantitatively understand the influence of turbulence and presence of neighboring bubbles on drag acting on bubbles. This submodel was used to identify an appropriate correlation for estimating the interphase drag force. The standard k–ε turbulence model was used to simulate turbulent gas–liquid flows in a stirred vessel. A computational snapshot approach was used to simulate motion of the standard Rushton turbine in a fully baffled vessel. The computational model was mapped onto FLUENT4.5, a commercial CFD solver. The model predictions were compared with the previously published experimental data of Bombac and co-workers. The model was used to simulate three distinct flow regimes in gas–liquid stirred vessels: vortex clinging (VC), alternating small cavities (S33), and alternating large cavities (L33). The predicted results show reasonably good agreement with the experimental data for all three regimes. The computational model and results discussed in this work would be useful for understanding and simulating gas holdup distribution and flow regimes in stirred vessels. © 2006 American Institute of Chemical Engineers *AIChE J,* 52: 1654–1672, 2006
Keywords: stirred vessel, Rushton turbine, computational fluid dynamics (CFD), gas holdup distribution, flow regimes

Introduction

Reactions between gas and liquid phases are commonly carried out in chemical and allied industries. Stirred vessels are widely used to carry out these reactions because they offer unmatched flexibility and control to tailor their fluid dynamics. To derive the benefits of the degrees of freedom offered by stirred reactors, it is essential to establish a relationship between process performance and fluid dynamics, on the one hand, and hardware configuration and operating conditions with fluid dynamics, on the other hand—the latter of which is the focus of this article.

Despite the widespread use of stirred vessels, the relationship between fluid dynamics and hardware is not adequately understood. Design engineers are still compelled to use empirical information. This is especially true for multiphase flows in stirred vessels. Gas–liquid flows in a stirred vessel exhibit different flow regimes depending on scale, impeller details (type, diameter, location, rotational speed), and gas flow rate. In this work, the scope is restricted to the study of gas–liquid flows generated by the standard Rushton turbine in a fully baffled vessel. Traditionally, empirical correlations are used to estimate prevailing flow regimes and corresponding flow characteristics. For example, Warmoeskerken and Smith[1] presented a flow regime map for gas–liquid flows generated by a single Rushton turbine in a fully baffled vessel. The map (shown in Figure 1) shows four main flow regimes: (1) vortex clinging (VC) cavities, (2) three large and three-vortex clinging (S33) cavities, (3) three large and three small (L33) cavities, and (4) ragged cavity (RC) structures. Flow characteristics of these regimes differ significantly. Empirical correlations are also used to estimate overall/global parameters characterizing the

Correspondence concerning this article should be addressed to V. V. Ranade at vv.ranade@ncl.res.in.

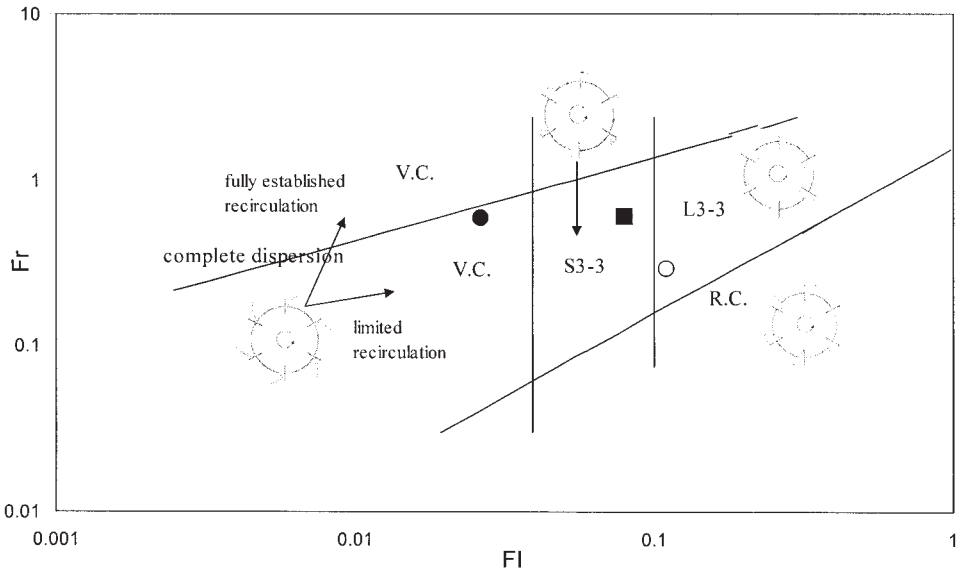

Figure 1. Flow regime map for Rushton turbine (from Warmoeskerken and Smith[1]).

Symbols denote operating conditions selected for simulation.

flow (such as power dissipation, volume fraction, mixing time, and so on). However, such overall characteristics conceal variations within the vessel. Such localized information may be crucial for successful design of process equipment (such as avoiding oxygen starvation in oxidation reactor). Besides this, availability of the relevant empirical information is often a problem, arising from either the cost or the constraints on time. Considering this, it would be most useful to develop computational models, which will allow prediction of detailed quantitative information about the prevailing flow characteristics. In this work, such an attempt is made.

A brief review of recent literature shows substantial progress in simulating flows in stirred vessels using computational fluid dynamics (CFD). CFD models were shown to be successful in simulating single-phase flow generated by impeller(s) of any shape in complex vessels.[2] For multiphase flows, the complexity of modeling increases considerably and this remains an area for further research and development. Despite the complexity, several attempts have been made to simulate the gas–liquid flows in stirred vessels.[3-14] Although some degree of success is reported, a number of limitations are apparent.

Earlier studies were carried out with a rather inadequate number of computational cells and were qualitative in nature.[3,6] Most of the published simulations used a single bubble diameter for the whole vessel. Recently, Laakkonen et al.[12] and Lane et al.[14] used a variable bubble size model based on coalescence and breakage processes. These multifluid models with coalescence–breakup processes increase the demands on computational resources by an order of magnitude and are often forced to use an appreciably smaller number of computational cells (<80,000 cells). Adequate grid resolution (usually >300,000 cells), however, is essential to correctly simulate flow around impeller blades.[15] Ranade and Deshpande[7] and Ranade et al.[10] studied the influence of gas flow rate on the trailing vortices of a Rushton turbine. The predicted results showed the accumulation of gas behind the impeller blades. However, the focus was on the near-impeller region; whether the models are able to simulate different flow regimes quantitatively was not studied.

Apart from the simulation of trailing vortices and flow around impeller blades, the published studies also highlight the importance of appropriate interphase drag force formulation.[5,9,14,16,17] Interphase drag coefficient was found to affect both, the distribution of gas holdup and total holdup of gas. Although several correlations are available to estimate interphase drag coefficient, adequate guidelines to select the appropriate model for interphase drag force for all the regimes of gas–liquid flow in a stirred vessel are not available. It is necessary to systematically evaluate these different interphase drag force models with respect to different flow regimes in gas–liquid stirred vessels. None of the previous studies was able to quantitatively simulate different prevailing flow regimes. Such an attempt is made here. In this work, we have selected the experimental data of Bombac et al.,[18] who used a phase-detection technique to identify flow regimes and have provided one of the most detailed data sets on gas holdup distribution within the vessel. The computational model developed herein was therefore used to simulate gas–liquid flow in the experimental setup used by Bombac et al.[18] The model predictions were evaluated by comparing predictions with the experimental data over three different flow regimes.

Mathematical Modeling

Model equations

In a gas–liquid stirred vessel, the sparged gas interacts with the trailing vortices behind the impeller blades and forms gas cavities behind impeller blades. The cavities are then sheared at the tips and smaller bubbles are formed that are dispersed in the vessel. The size of the bubbles emanating from the cavity tip is controlled by the size of the cavity, breakage of the cavity, and the turbulence level around the cavity. Unfortunately, no direct experimental data for turbulent kinetic energy dissipation rate are available for validating the available cavity breakage mod-

els. In principle, cavity formation behind impeller blades and their shearing at the tip can be simulated by using a volume of fluid (VOF) approach. The first attempt to carry out such simulations was made some years ago.[19] Unfortunately, the computing demands for such simulations are enormous and it was not possible to accurately track the formation of smaller bubbles. It is unrealistic at present to extend such models for simulating gas–liquid flow in stirred vessels. Therefore, in the present study the Eulerian–Eulerian approach was used.

In a gas–liquid stirred vessel, gas bubbles of different sizes coexist. Very fine bubbles are observed in the impeller discharge stream (<1 mm), whereas bubbles a few millimeters (~5 mm) of size are observed in the region away from the impeller.[20] The width of bubble size distribution depends on the turbulence level and prevailing flow regime. Considering the importance of the right prediction of slip velocity, it might be necessary to use appropriate bubble sizes. The multifluid model with appropriate breakage and coalescence rates, which is able to simulate evolution of bubble size distribution within the vessel, may provide a better way to simulate the gas–liquid flow in stirred vessels.[21] Unfortunately, a single comprehensive data set on bubble size distribution is not available in the literature.[20] However, the available experimental data are not sufficient to calculate the parameters appearing in coalescence and breakup kernels.

Apart from the uncertainties in parameters of coalescence and breakup kernels and cavity modeling, there is significant uncertainty in estimation of interphase forces on gas bubbles in the presence of other bubbles and high levels of turbulence prevailing in the vessel. Considering these issues and the present state of understanding, the option of using multifluid computational model for stirred vessels, which requires an order of magnitude more computational resources, was deemed to be ineffective. Instead, an approach of using a two-fluid model with a single bubble size for the whole vessel (and lump all the uncertainties into the interphase drag coefficient) was adopted here. The bubble size used in the present study and the basis for selection of the bubble size are discussed in the next subsection.

For most of the operating regimes shown in Figure 1, gas–liquid flows in stirred vessel are turbulent. Therefore, the Reynolds-averaged mass and momentum balance equations for each phase in turbulent flow regime were expressed as (without considering mass transfer)

$$\frac{\partial(\alpha_q\rho_q)}{\partial t} + \nabla\cdot(\alpha_q\rho_q\vec{U}_{q,i} - \rho_q D_{12}\nabla\alpha_q) = 0 \qquad (1)$$

$$\frac{\partial(\alpha_q\rho_q\vec{U}_{q,i})}{\partial t} + \nabla\cdot(\alpha_q\rho_q\vec{U}_{q,i}\times\vec{U}_{q,i}) = -\alpha_q\nabla\vec{p} - \nabla\cdot[\alpha_q\bar{\bar{\tau}}^{(lam)}_{q,ij}] - \nabla\cdot[\alpha_q\bar{\bar{\tau}}^{(t)}_{q,ij}] + \alpha_q\rho_q g_i + \vec{F}_{12,i} \qquad (2)$$

Here $q = 1$ and $q = 2$ denote the continuous phase (liquid) and the dispersed phase (gas), respectively; i is the direction. $\vec{U}_q$ and α_q are the time-averaged values of the velocity and volume fraction of phase q, respectively. It should be noted that time-averaged pressure ($\vec{p}$) is shared by both phases and, therefore, appears in the governing equations of all the phases. ρ_q is the density of phase q and D_{12} is the turbulent diffusivity of dispersed phase. $\vec{F}_{12,i}$ is the time-averaged interphase force in the i direction and is discussed later in this section. $\alpha_q\rho_q g_i$ is the external body force on phase q. $\bar{\bar{\tau}}^{(lam)}_{q,ij}$ is the stress tensor in phase q arising from the viscosity and $\bar{\bar{\tau}}^{(t)}_{q,ij}$ is the Reynolds stress tensor of phase q (representing contributions of correlation of fluctuating velocities in momentum transfer). In this work, we used Boussinesq's eddy viscosity hypothesis to relate the Reynolds stresses with gradients of time-averaged velocity as

$$\bar{\bar{\tau}}^{(t)}_{q,ij} = \mu_{tq}\left\{[\nabla\vec{U}_{q,i} + (\nabla\vec{U}_{q,i})^T] - \frac{2}{3}I(\nabla\vec{U}_{q,i})\right\} \qquad (3)$$

Here, μ_{tq} is the turbulent viscosity of phase q and I is the unit tensor. Despite the known deficiencies, the overall performance of the standard k–ε turbulence model for simulating flows in stirred vessels is adequate for many engineering applications.[2] In the present work, we have therefore used the standard k–ε turbulence model to estimate the turbulent viscosity of the liquid phase. The governing equations for turbulent kinetic energy (k) and turbulent energy dissipation rate (ε) were solved only for the liquid phase and are listed below:

$$\frac{\partial}{\partial t}(\alpha_l\rho_l\phi_l) + \nabla\cdot(\alpha_l\rho_l\vec{U}_{l,i}\phi_l) = -\nabla\cdot\left(\alpha_l\frac{\mu_{tl}}{\sigma_{\phi l}}\nabla\phi_l\right) + S_{\phi,l} \qquad (4)$$

where ϕ_l can be the turbulent kinetic energy or the turbulent energy dissipation rate in the liquid phase. The symbol $\sigma_{\phi l}$ denotes the turbulent Prandtl number for variable ϕ. $S_{\phi l}$ is the corresponding source term for ϕ in the liquid phase. Source terms for turbulent kinetic energy and dissipation can be written as

$$S_{kl} = \alpha_l[(G_l + G_{el}) - \rho_l\varepsilon_l]$$
$$S_{\varepsilon,l} = \alpha_l\frac{\varepsilon_l}{k_l}[C_1(G_l + G_{el}) - C_2\rho_l\varepsilon_l] \qquad (5)$$

where G_l is generation in the liquid phase and G_{el} is extra generation (or dissipation) of turbulence in the liquid phase. Generation attributed to mean velocity gradients G_l and turbulent viscosity $\mu_{t,l}$ was calculated as

$$G_l = \frac{1}{2}\mu_{tl}[\nabla\vec{U}_{l,i} + (\nabla\vec{U}_{l,i})^T]^2 \qquad \mu_{tl} = \frac{\rho_l C_\varpi k_l^2}{\varepsilon_l} \qquad (6)$$

Extra generation or damping of turbulence resulting from the presence of dispersed-phase particles is represented by G_{el}. Kataoka et al.[22] analyzed the influence of the gas bubbles on liquid phase turbulence. The motion of larger bubbles generates extra turbulence. However, their analysis indicates that the extra dissipation arising from small-scale interfacial structures almost compensates the extra generation of turbulence arising from large bubbles. Numerical experiments on bubble columns also indicate that one may neglect the contribution of extra turbulence generation.[23] Therefore, in the case of stirred vessels, where impeller rotation generates significantly higher turbulence than that observed in bubble columns, the contribu-

tion of the additional turbulence generation arising from bubbles can be neglected. In the present work, therefore, G_{el} was set to zero. Standard values of the k–ε model parameters were used in the present simulations. No separate equations were solved for modeling turbulence in the dispersed phase. Instead the turbulent viscosity of the dispersed phase was estimated from knowledge of turbulent viscosity of the liquid phase as

$$\mu_{tg} = \frac{\rho_g}{\rho_l}\,\mu_{tl} \tag{7}$$

In the Reynolds averaging procedure, turbulent dispersion of the dispersed phase was modeled using the turbulent diffusivity D_{12} in the mass balance equation (Eq. 1). The numerical study of Khopkar et al.[11] indicated that the turbulent dispersion terms were significant only in the impeller discharge stream. Even near the impeller, the influence of dispersion terms on predicted results was not quantitatively significant (difference was $<5\%$). It should be noted that only turbulent eddies larger than the bubble diameter will contribute to dispersion. Under the usual operating conditions of gas–liquid flow in laboratory-scale stirred vessels (with smaller impeller blades leading to smaller scales of energy containing eddies), the contribution of eddies larger than bubbles is unlikely to be significant. Considering these results, turbulent dispersion of the dispersed phase was not considered in the present study (the third term in the left-hand side of Eq. 1 was neglected).

Interphase coupling terms make two-phase flows fundamentally different from single-phase flows. The formulation of time-averaged $\vec{F}_{12,i}$, therefore, must proceed carefully. The interphase momentum exchange term consists of four different interphase forces: Basset history force, lift force, virtual mass force, and drag force.[24] Basset force arises as a result of the development of a boundary layer around bubbles and is relevant only for unsteady flows. Basset force involves a history integral, which is time-consuming to evaluate and, in most cases, its magnitude is much smaller than the interphase drag force. Bubbles undergo lift force as a result of vorticity and shear in continuous phase flow field. Lift force is proportional to the vector product of the slip velocity and the curl of liquid velocity. Lift force is significant if the velocity gradients are large. In stirred vessels, velocity gradients are significant mainly near the impeller. In the bulk region of the vessel, the velocity gradients are not large. In the vicinity of the impeller, pressure gradients and interphase drag forces would mainly dominate the motion of bubbles. An order of magnitude analysis indicates that the magnitude of lift force is much smaller than the interphase drag force.[9] The virtual mass force needs to be considered when a secondary phase accelerates relative to the primary phase. It becomes significant when the secondary phase density is much smaller than the continuous phase density (as in gas–liquid stirred vessel or bubble column reactor). Considering this, in the present work, Basset and lift forces were not considered. The virtual mass and drag force terms were included in the interphase momentum exchange term as

$$\vec{F}_{12,i} = \vec{F}_{D,i} + \vec{F}_{VM,i} \tag{8}$$

The virtual mass term in the i direction is given as

$$\vec{F}_{VM,i} = \alpha_2\rho_1 C_{VM}\left(\frac{D\vec{U}_{2,i}}{Dt} - \frac{D\vec{U}_{1,i}}{Dt}\right) \tag{9}$$

where C_{VM} is the virtual mass coefficient. In the present work, the value of C_{VM} was set to 0.5.

The interphase drag force exerted on phase 2 in the i direction is given by

$$\vec{F}_{D,i} = -\frac{3\alpha_1\alpha_2\rho_1 C_D[\Sigma\,(\vec{U}_{2,i} - \vec{U}_{1,i})^2]^{0.5}(\vec{U}_{2,i} - \vec{U}_{1,i})}{4d_b} \tag{10}$$

As discussed earlier, the estimation of drag force is critical for accurate prediction of gas distribution within stirred vessels. Most of the available correlations to estimate drag coefficient appearing in Eq. 10 relate the value of drag coefficient to bubble Reynolds number. These correlations are valid for a single bubble rising in a stagnant liquid. In this work, the value of drag coefficient for a single bubble rising in a stagnant liquid, C_{D0}, was estimated using the following correlation of Tsuchiya et al.[25]:

$$C_{D0} = \max\left\{\left(\frac{2.667\mathrm{Eo}}{\mathrm{Eo} + 4.0}\right), \left[\frac{24}{\mathrm{Re}_b}(1 + 0.15\mathrm{Re}_b^{0.687})\right]\right\} \tag{11}$$

It is likely that the presence of neighboring bubbles affects the drag coefficient of a bubble. Ishii and Zuber[26] studied the effect of neighboring particles or bubbles on drag coefficient and proposed a correction factor as the square of continuous phase holdup. Gas volume fraction in the bulk region of the tank is $<5\%$ in most of the cases studied by Bombac et al.[18] For such situations, the magnitude of the drag reduction correlation estimated by Ishii and Zuber[26] is $<10\%$. Therefore, in this work the correction factor attributed to the presence of other bubbles was not considered. Unlike a case of a bubble flowing through stagnant liquid, where flow around a bubble is dominated by motion of that bubble, in stirred vessels, bubbles undergo significantly higher turbulence generated by impellers. Unless the influence of this prevailing turbulence on bubble drag coefficient is accounted for, the CFD model will not adequately predict the pattern of gas holdup distribution. Relatively few attempts (experimental as well as numerical) have been made to understand the influence of prevailing turbulence on drag coefficient.[5,14,16,17,27] Bakker and van den Akker,[5] Brucato et al.,[16] and Lane et al.[14] all attempted to relate the influence of turbulence on drag coefficient to the characteristic spatiotemporal scales of prevailing turbulence, which is a promising development. These are briefly discussed here.

Bakker and van den Akker[5] attempted to relate the influence of turbulence on drag coefficient by using a modified Reynolds number in a usual correlation developed for the stagnant liquid. Their proposal is expressed as

$$C_D = \frac{24}{\mathrm{Re}^*}[1 + 0.15(\mathrm{Re}^*)^{0.687}] \qquad \because \mathrm{Re}^* = \frac{\rho_l U_{slip} d_b}{\mu_l + \frac{2}{9}\mu_t} \tag{12}$$

It should be noted that the effective viscosity is calculated by adding some fraction of turbulent viscosity to the molecular viscosity. The fraction is an adjustable parameter and the value of 2/9 is recommended.

Brucato et al.[16] attempted to relate the influence of turbulence on drag coefficient to the ratio of the particle size and the Kolmogorov length scale of the turbulence (based on their experiments with solid particles in a Taylor–Couette apparatus) as

$$\frac{C_D - C_{D0}}{C_{D0}} = K\left(\frac{d_b}{\lambda}\right)^3 \tag{13}$$

where C_D is the drag coefficient in turbulent liquid, C_{D0} is the drag coefficient in stagnant liquid, d_b is bubble/particle diameter, and λ is the Kolmogorov length scale (based on volume-averaged energy dissipation rate). It should be noted that the flow field around bubbles, which essentially controls interphase drag would be affected not by inertial scale turbulence but by microscale turbulence. It thus appears logical that the interphase drag coefficient is affected by microscales. Experimental data of Brucato et al.[16] clearly indicate that only microscale turbulence affects the particle drag. The correlation constant K was reported to be 8.67×10^{-4}. It should be noted that despite significantly nonuniform distribution of ε in a Taylor–Couette apparatus, the correlation was based on volume-averaged energy dissipation rate. This makes the direct extension of the correlation to different configurations difficult and may necessitate use of a different multiplier than that proposed by Brucato et al.[16] The experimental data presented by Brucato et al.[16] also clearly show a systematic trend of decreasing the value of multiplier with increase in particle size (see Figure 11 of Brucato et al.,[16] where particles of 63–71, 212–250, and 425–500 microns show trends with decreasing intercept with increasing particle size). This trend indicates that the value of K for bubbles (which are much larger than the solid particles considered in their work) will be much lower than that proposed by Brucato et al.[16] A recent study reported by Lane et al.[9] also supports the lower value of K. Lane et al.[9] found better agreement with experimental data using a 100 times smaller value of K, although no clear guidelines are available on deciding the appropriate value of K.

Recently, Lane et al.[14] correlated the available data of settling velocity of particles and rise velocity of bubbles in a turbulent flow with particle relaxation time (τ_p) and integral timescale of turbulence (T_L) as

$$\frac{C_D}{C_{D0}} = \left[1 - 1.4\left(\frac{\tau_p}{T_L}\right)^{0.7} \exp\left(-0.6\,\frac{\tau_p}{T_L}\right)\right]^{-2} \tag{14}$$

The experimental data used for correlation was taken with particle or bubble sizes < 1000 microns. The adequacy of the proposed correlation for larger particles of size 4000 microns is not known. The proposed correlation predicts the drop in drag coefficient values for higher values of ratio of two timescales. No experimental data supporting this trend were reported.

Considering the importance of accurate accounting of prevailing turbulence in simulation of gas–liquid flow in stirred vessels, a computational submodel was developed in the present study. Previous literature suggested that the increase in drag coefficient might be attributable to the dynamic interaction of accelerating bubbles/particles and a turbulent flow field. The detailed direct numerical simulations or lattice Boltzmann simulations can provide unambiguous information for understanding various possible mechanisms of increase in drag on moving bubbles,[28] although it is impractical to carry out such detailed simulations of gas–liquid flow in stirred reactors where millions of bubbles coexist. To address such practical flow problems, several attempts have been made to represent the complex dynamic interactions of moving bubbles with the surrounding turbulence by using time-averaged quantities. For example, Clift et al.[29] represented the influence of prevailing turbulence intensity (time-averaged quantity) on drag exerted on particles. More recent attempts have also correlated their experimental data with time-averaged quantities without any explicit reference to real-life dynamic interactions.[5,14,16] The key length and timescales of prevailing turbulence were estimated using time-averaged quantities such as turbulence kinetic energy and turbulent energy dissipation rate. Because most of the previous attempts of representing the influence of turbulence used time-averaged quantities, ignoring dynamical interactions of dispersed particles with surrounding turbulence, in the present study a model problem of steady flow of liquid over a regular array of bubbles was thus considered. Even if this approach cannot provide information on dynamic interactions, a critical analysis of previous attempts indicates that this might be an adequate method for representing the influence of turbulence on dispersed particles/bubbles in framework adapted in the present work.

The preliminary simulations were first carried out to evaluate possible differences in the flow over a regular array of cylinders and flow over a regular array of spheres [which needs to be simulated using three-dimensional (3D) solution domain]. It was observed that the predicted values of relative drag coefficient for the two-dimensional (2D) and 3D cases were not significant (these results are discussed later). Based on these results, 2D cases were further investigated to reduce demands on computational resources without jeopardizing the relevance. The flow was then modeled in a 2D solution domain using a "unit cell " approach (discussed later in more detail). This means, flow through a bank of regularly arranged cylinders was computationally studied. Various influences of Reynolds number, volume fraction of bubbles, and prevailing turbulence level on drag coefficient were investigated. The standard k–ε turbulence model was used to simulate the turbulence in the flow. The level of prevailing turbulence was varied by specifying different magnitudes of additional source for turbulence generation by the following expression:

$$G = \frac{1}{2}\,\mu_t[\nabla \vec{U}_i + (\nabla \vec{U}_i)^T]^2 + f \tag{15}$$

where f is the extra source of turbulence. By manipulating the value of such extra source, volume-averaged values of turbulent viscosity, Kolmogorov length scales, and integral timescales of turbulence were varied over a range of interest. The predicted results on drag coefficients were thus used to identify an appropriate correlation for estimating interphase drag force on bubbles in turbulent flow. The developed correlation was

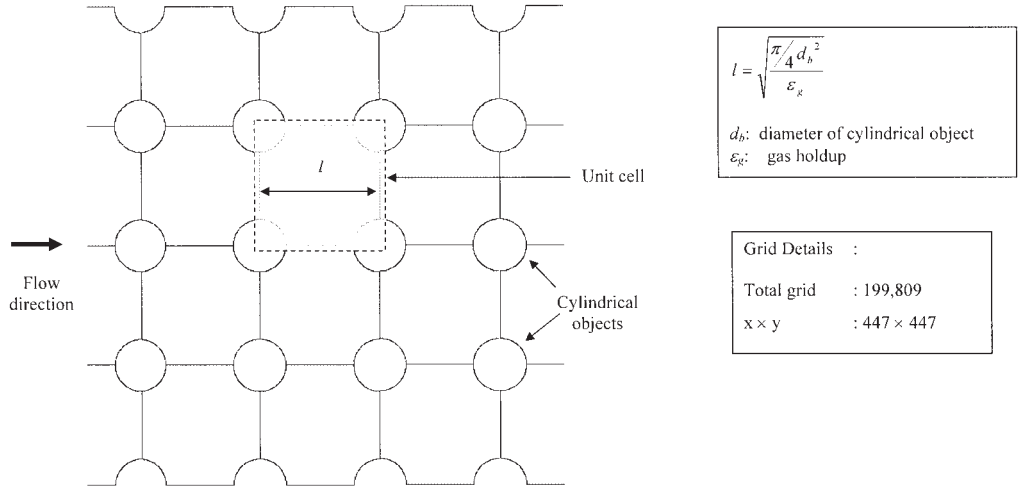

Figure 2. Solution domain for flow through regular array of cylinders.

then evaluated for simulating gas–liquid flow in a stirred vessel by comparing simulated results with the experimental data of Bombac et al.[18]

The gas–liquid flow in stirred vessel was simulated using the computational snapshot approach, in which impeller blades are considered as fixed at one particular position (similar to taking a snapshot of a rotating impeller) with respect to baffles. The blade rotation causes suction of fluid at the backside of blades and an equivalent ejection of fluid from the front side of the blades. This phenomenon of ejection and suction is modeled by specifying appropriate sources and sinks for all the variables. No empirical information is needed to specify these sources or sinks and the approach is mathematically equivalent to the more commonly used multiple reference frame (MRF) approach. Recently, Ranade[2] discussed the development of snapshot approach in detail and therefore it will not be discussed here.

It should be noted that in quasi-steady-state approaches, such as the computational snapshot approach, a specific position of the impeller blades with respect to other stationary internals is considered. The choice of blade positions with respect to baffle positions is rather arbitrary. However, in most experimental studies, flow measurements were carried out in a fixed position for several rotations of the impeller. Thus, the measured flow characteristics were essentially averaged over different relative impeller blade positions. To make meaningful comparisons, it would be necessary to carry out simulations at different blade positions and then use ensemble-averaged results over these different simulations for comparison. Ranade and van den Akker[6] studied the sensitivity of simulated results with the exact position of blades relative to baffles by comparing predicted results of five snapshots. They compared ensemble-averaged results (over five snapshots) for the midbaffle plane with angle-averaged results. Their results indicate that, although local values may differ for different relative positions, angle-averaged results are not sensitive to the actual positioning of impeller blades. Predicted values of overall characteristics such as pumping number and power number are also not sensitive to relative positions of impeller blades and baffles. Therefore, only one snapshot was considered in the present work and angle-averaged values were predicted with the available experimental data.

Solution domain and boundary conditions

Flow through Regularly Arranged Cylindrical Objects. A "unit cell " approach was used to model the single-phase flow through regularly arranged cylindrical objects (applicability of unit cell approach to model flows through regular array is recently discussed by Gunjal et al.[30]). Cylinders were arranged in a regular square array (see Figure 2). The spacing between the cylinders was calculated by specifying the relevant value of volume fraction. Figure 2 shows cylindrical objects having diameter (d_b) equal to 5×10^{-3} m with volume fraction equal to 15%. The unit cell approach uses the geometrical symmetry to significantly reduce the computational requirements (also shown in Figure 2). All sides of the unit cell were defined as periodic walls. Considering the negligible shear exerted by the gas flow within a bubble on the surrounding liquid, the walls of cylindrical objects were defined as zero shear walls. Simulations were carried out for different Reynolds numbers (by specifying different values of liquid mass flow rates through the unit cell), volume fractions (by considering different geometries), and levels of prevailing turbulence (by specifying different magnitudes of extra generation, f). In a stirred reactor the bubble Reynolds number varies in the range of 200 to 800. The mass flow rate of the liquid was then calculated as

$$u_\infty = \frac{\mathrm{Re}\ \mu}{\rho d_b} \qquad m = \rho u_\infty A_f \tag{16}$$

where A_f is the flow area ($\propto l$ shown in Figure 2) and m is the mass flow rate of the liquid. The direction of net flow of liquid was set as shown in Figure 2. The simulations were carried out for three Reynolds numbers (200, 500, and 800) and for two values of volume fraction of gas (5 and 15%). The turbulent flow around the cylinders with zero shear walls was simulated using FLUENT 6.1.22 (Fluent Inc., Lebanon, NH). The magnitude of f was varied in the range of 0 to 5000 kg s^{-3} m^{-1} to

cover the variation of the Kolmogorov length scale between 1×10^{-4} and 1×10^{-6} m, as usually observed in stirred vessels.

The prediction of flow characteristics, especially turbulence quantities, is sensitive to the number of grid nodes, grid distribution within the solution domain, and the discretization scheme. In the present work, we used the QUICK (Quadratic Upstream Interpolation for Convective Kinetics) discretization scheme with limiter function (SUPERBEE) to avoid nonphysical oscillations. A commercial grid-generation tool, GAMBIT 2.0 (Fluent Inc.) was used to model the geometry and to generate the body-fitted grids. The geometry was modeled with eight different grid size distributions with total number of computational cells ranging from 5000 to 800,000. The predicted results are discussed in the next section.

Gas–Liquid Stirred Vessel. In the present work, the experimental setup used by Bombac et al.[18] was considered. All the relevant dimensions such as impeller diameter, impeller off-bottom clearance, vessel height and diameter, sparger location and diameter, and so on were the same as those used by Bombac et al.[18] The absence/presence of bottom bearing was assumed to have a negligible effect on the gas holdup distribution pattern. Thus, to simplify the modeling geometry, the bottom bearing was not considered herein. The system investigated consists of a cylindrical, flat-bottom vessel (diameter, $T = 0.45$ m; height, $H = 0.45$ m). Four baffles of width $T/12$ were mounted perpendicular to the vessel wall with a gap of 0.007 m. The shaft of the impeller was concentric with the axis of the vessel and extended to the bottom of the vessel. A standard Rushton turbine (diameter, $D_i = T/3$) was used for all simulations. The impeller off-bottom clearance ($C = T/4$) was measured from the bottom of vessel.

Considering the symmetry of geometry, half of the vessel was considered as a solution domain (see Figure 3). It should be noted that, even if the geometry is symmetric, the flow might not be symmetric. For example, flow regimes S33 and L33 do not exhibit half-plane symmetry. The physical reasons for possible asymmetry in cavity shapes are not yet clear. Therefore, in the present work, simulations were carried out with half of the vessel to reduce computational demands. The objective was to examine whether the computational model is able to correctly capture the variation of gas accumulation for different flow regimes if not the asymmetry. The baffles were considered at angles of 45 and 135°. The impeller was positioned in such a way that three blades were located at angles of 30, 90, and 150°. As discussed by Ranade,[2] the computational snapshot approach divides the solution domain in an inner region, in which time-derivative terms are approximated using spatial derivatives and an outer region, in which time derivative terms are neglected. The boundary between the inner and outer region needs to be selected in such a way that the predicted results are not sensitive to its actual location. Fortunately, for the standard impellers with impeller diameter of about one third of vessel diameter, the predicted results are not sensitive to actual location of boundary between the inner and outer regions.[2] In the present work, for all simulations, the boundary of the inner region was positioned at $r = 0.138$ m and 0.09 m $\leq z \leq 0.265$ m (where z is axial distance from the bottom of the vessel).

The ring sparger (diameter, $d_{sp} = T/3$) was located at 0.075 m from the bottom of the vessel. The sparger was modeled as a solid wall and a mass source for the gas phase was specified one cell above the sparger to simulate gas introduction in vessel. Special boundary conditions are needed to simulate the gas–liquid interface at the top through which bubbles escape the solution domain. Recently, Ranade[2] discussed different possible approaches to treat the gas–liquid interface in detail. We have modeled the top surface of the dispersion as velocity inlet. The outgoing (axial) velocity of gas bubbles was set equal to the terminal rise velocity of gas bubbles (estimated as 0.2 m/s for air bubbles). Normal liquid velocity was set to zero. The implicit assumption here is that gas bubbles escape the dispersion with terminal rise velocity. Because the liquid velocity near the top gas–liquid interface is small and the overall volume fraction of gas is also small (<5%), this assumption is reasonable. It should be noted that even after defining the top surface as an inlet, the gas volume fraction at the top surface is a free variable.

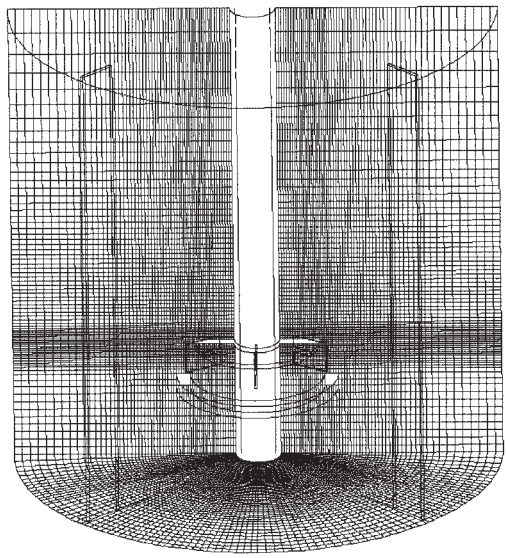

Figure 3. Computational grid and solution domain of stirred vessel.

It would have been appropriate to specify the value of effective bubble size in the computational model by using experimental data. Unfortunately, Bombac et al.[18] did not measure the bubble size distribution in their experimental study. Barigou and Greaves[20] reported experimentally measured bubble size distribution for the stirred vessel of diameter 1 m [of size $T = H = 1$ m, $C = T/4$, and $D_i = T/3$; operating range, Froude number (Fr): 0.37–0.765; flow number (Fl): 0.015–0.06]. Their experimental data clearly indicate that the bubble size in the bulk region of the vessel varies between 3.5 and 4.5

mm for high gas flow rate. The reported values of Sauter mean diameter, D_{32}, for the cases relevant to those studied by Bombac et al.[18] are about 4 mm ($D_{32} = 3.75$ mm for Fl = 0.04 and Fr = 0.765 and $D_{32} = 4.24$ mm for Fl = 0.056 and Fr = 0.37). We have thus used the effective bubble size as 4 mm for the S33 and L33 regimes. For the VC regime, where higher impeller speed was used, a bubble size of 3 mm was used in the simulations. Fluid properties were set as those of water and air for the primary and secondary phases, respectively.

It is very important to use an adequate number of computational cells while numerically solving the governing equations over the solution domain. The prediction of turbulence quantities is especially sensitive to the number of grid nodes and grid distribution within the solution domain. Our previous work[10] as well as other published work[31,32] gives adequate information to understand the influence of number of grids on the predicted results. It was demonstrated that, to capture the details of flow near impeller, it is necessary to use at least 200 grid nodes to resolve the blade surface. Based on previous experience and some preliminary numerical experiments, the numerical simulations for gas–liquid flows in stirred vessel for all three operating conditions were carried out for grid size ($r \times \theta \times z$: 63 × 98 × 82). In the present work we have used ($r \times \theta \times z$: 18 × 1 × 19) grid nodes covering the impeller blade. The boundary of the inner region was positioned at $j \leq 45$ and $15 \leq k \leq 65$ (where j is cell number in radial direction from shaft and k is cell number in the axial direction from the bottom of vessel). The computational grid used in the present work is shown in Figure 3. In the present work, the QUICK discretization scheme with SUPERBEE limiter function (to avoid nonphysical oscillations) was used. Standard wall functions were used to specify wall boundary conditions. The computational results are discussed next.

Results and Discussion

Influence of prevailing turbulence on drag coefficient

Preliminary simulations of flow through regularly arranged cylindrical objects were first carried out for all eight grid size distributions, varied from 5000 to 800,000 computational cells. Based on these numerical simulations, it was found that about 200,000 computational cells were sufficient to adequately predict the flow (the difference between the predicted values of pressure drop for 200,000 and 800,000 grid nodes was found to be within 7% of the pressure drop value for 800,000 grid nodes). Therefore, all further simulations were carried out with the grid size of about 200,000. Typical predicted results for the porosity equal to 85%, Reynolds number equal to 200, and without any source for extra turbulence are shown in Figure 4 in the form of velocity vectors and the contours of predicted pressure and turbulent kinetic energy. The predicted velocity field around the cylindrical objects is shown in Figure 4a(i). The predicted velocity field shows the presence of wake behind the cylindrical objects. The predicted pressure and turbulent kinetic energy distribution around the cylindrical objects are shown in Figures 4b(i) and 4c(i), respectively. The predicted results show the presence of a high-pressure and high turbulent kinetic energy region near the nose of the cylindrical objects. The approach and computational models were validated (not shown here for the sake of brevity) by comparing predicted results with published correlations.[33,34] The computational model was then extended to understand the influence of free stream turbulence on the bubble drag coefficient.

An additional source for turbulent kinetic energy was specified using a user-defined function to simulate the presence of extra turbulence in a flowing liquid. The magnitude of this source term was varied to cover the variation of Kolmogorov length scales of turbulence in the range of 1×10^{-4} to 1×10^{-6}, as usually observed in stirred vessels. The predicted results show a significant increase in pressure drop values with increasing level of turbulence. A comparison of the predicted results for with and without extra turbulence (Figure 4) shows a significant change in the flow field around the cylindrical objects. As the level of prevailing turbulence increases, the high-pressure region in front of the cylinders increases, resulting into higher form drag. Values of drag coefficients for these different cases were calculated from the predicted pressure drop.[30] The predicted increase in drag coefficient with increase in prevailing turbulence is consistent with the previously reported experimental studies.[27,35,36]

It is worthwhile comparing the predicted fractional increase in the drag coefficient with the available approaches. Previous attempts to represent the influence of turbulence were based on turbulence viscosity,[5] Kolmogorov length scale,[16] and integral scale of turbulence.[14] The study reported by Brucato et al.[16] was restricted to a rather narrow range of particle Reynolds numbers [1–35] and therefore their correlation did not include particle Reynolds number as a relevant parameter. In contrast to this, the correlation proposed by Bakker and van den Akker[5] included particle Reynolds number as a relevant parameter. No information was available on elucidating the influence of various key time-averaged properties of prevailing turbulence on increase in drag on dispersed particles or bubbles. It was essential to evaluate these three approaches before selecting the most suitable approach. Direct evaluation of these three approaches by carrying out simulations of gas–liquid flow in stirred reactors would not have been very instructive, given that rather limited data in stirred reactor were available and in simulations of gas–liquid stirred reactors, several other possible uncertainties might evolve. Because none of these previous attempts of representing influence of prevailing turbulence on dispersed particles considered the dynamical interactions, as discussed above, in this work we have used the model predictions to evaluate the previous attempts. In the present submodel the values of the turbulence viscosity, Kolmogorov length scale, and integral scale of turbulence were varied over relevant ranges, by manipulating the additional source of turbulence generation, f. This approach allowed us to independently vary the relevant parameters and examine their influence on drag. The framework also allowed us to evaluate all three correlations on a uniform basis. The sample values of the turbulent kinetic energy, dissipation rate, integral timescale, turbulent viscosity, particle Reynolds number, particle response time, and so on for porosity equal to 85% and particle Reynolds number equal to 200 are listed in Table 1.

For quantitative analysis of influence of prevailing turbulence, the approach of Brucato et al.[16] was selected. The results predicted by the CFD model were compared with the available correlations[5,14,16,17] (Figure 5). The comparison brings out several salient points. The predicted increase in drag coefficient for the 3D cases (flow over spheres) is very similar to that observed for the 2D cases (flow over cylinders). It can also be

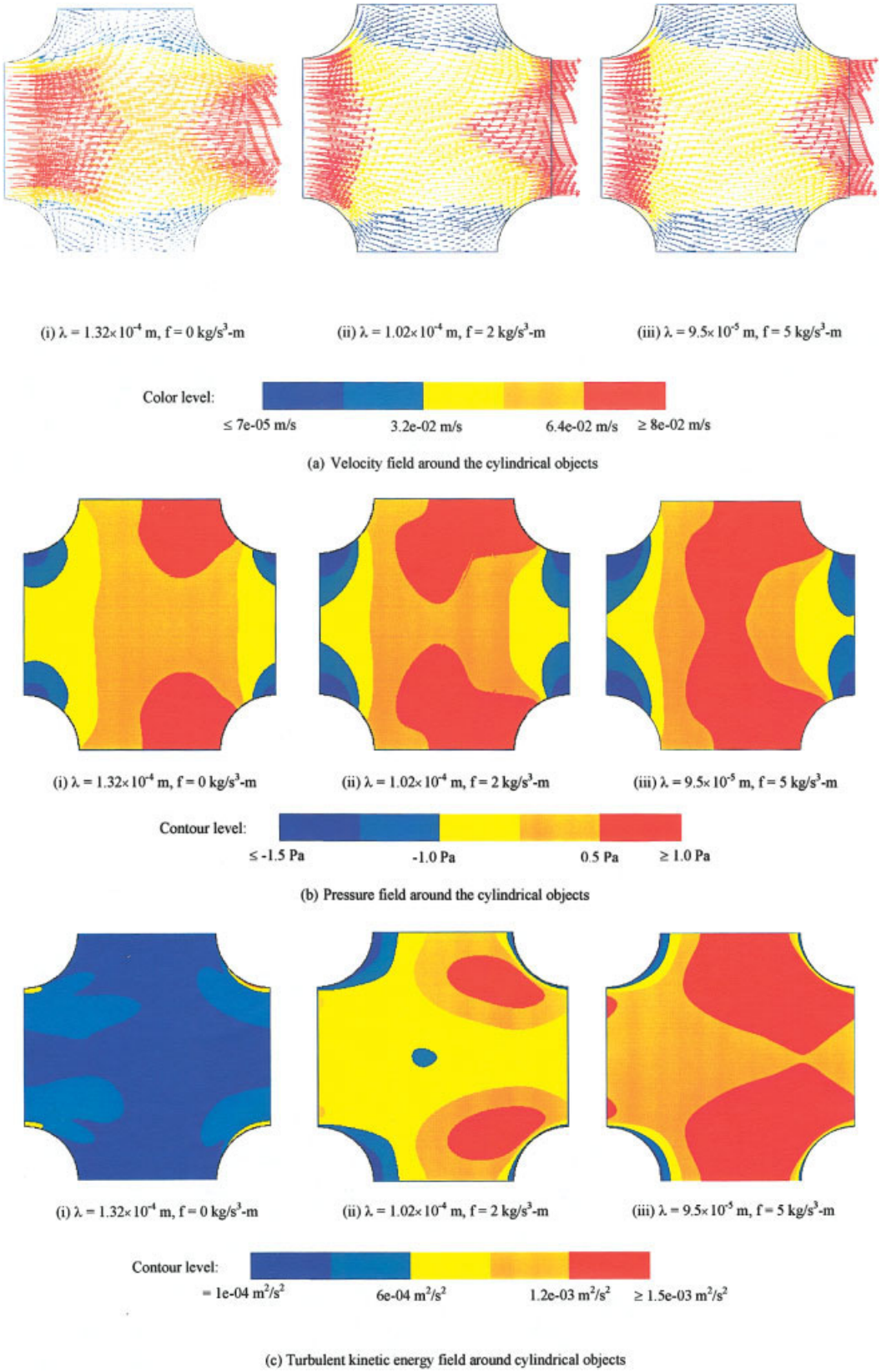

Figure 4. Simulated flow through array of cylinders.

(a) Velocity field around the cylindrical objects; (b) pressure field around the cylindrical objects; (c) turbulent kinetic energy field around cylindrical objects. [Color figure can be viewed in the online issue, which is available at www.interscience.wiley.com]

Table 1. Predicted Data from the Simulations of Flow through Array of Cylinders for Porosity = 85% and Re = 200

f (kg m^{-1} s^{-3})	k (m^2/s^3)	ε (m^2/s^2)	μ_t (kg m^{-1} s^{-1})	λ (m)	τ_p (s)	T_L(s)	$\frac{C_D - C_{D0}}{C_{D0}}$ Bakker and van den Akker	$\frac{C_D - C_{D0}}{C_{D0}}$ Lane et al.	$\frac{C_D - C_{D0}}{C_{D0}}$ Present Study
0	0.0002535	0.0023	0.0045	0.00014	0.0537	0.1102	—	—	—
5	0.00124	0.0123	0.0285	9.5×10^{-5}	0.0537	0.1008	1.81143	3.5833	1.465814
25	0.00189	0.0199	0.04634	8.42×10^{-5}	0.0537	0.095	2.36602	3.824	2.52382
500	0.00996	0.1687	0.2117	5.53×10^{-5}	0.0537	0.059	6.77	5.86	8.664976
5000	0.02812	0.8999	0.5111	3.25×10^{-5}	0.0537	0.03125	14.073	5.066	30.41037

seen from Figure 5 that the predicted values for the smaller solid (noted by solid triangles) particles (these simulations were carried out by following a similar approach with no-slip boundary conditions at the walls of cylinders) follow trends of correlation of Brucato et al.[16] As the Reynolds number increases, the predicted values shift toward the right, indicating a decrease in the magnitude of proportionality constant in the correlation of Brucato et al.[16] This is consistent with the experimental data reported by them. The predicted results deviate from the trends estimated by correlations of Pinelli et al.[17] and Lane et al.[14] for higher ratios of d_b/λ. These correlations were therefore not considered further.

The predicted results clearly indicate that in addition to d_b/λ, the fractional increase in drag coefficient is also a function of bubble Reynolds number and the volume fraction. The influence of volume fractions is not very significant for the considered ranges and was thus neglected in the present work. It can be seen from Figure 5 that the CFD predictions show reasonable agreement with the estimations based on correlation of Bakker and van den Akker.[5] While applying the correlation of Bakker and van den Akker[5] (Eq. 12), the volume-averaged value of turbulent viscosity was used. Importantly, this correlation captures the influence of Reynolds number on the impact of prevailing turbulence on drag coefficient. Considering the rather narrow range of Reynolds numbers relevant to gas–liquid flows in stirred vessels, the influence of Reynolds number might be ignored as done by Brucato et al.[16] The predicted results, however, require a much lower proportionality constant and can be correlated (modified correlation of Brucato et al.[16]) as

$$\frac{C_D - C_{D0}}{C_{D0}} = 6.5 \times 10^{-6}\left(\frac{d_b}{\lambda}\right)^3 \tag{17}$$

where C_D is the drag coefficient in turbulent liquid and C_{D0} is the drag coefficient in liquid without additional turbulence. The predictions of Eq. 17 are shown by the dotted line in Figure 5. The trends observed in the numerical results presented in Figure 5 support the reduced value of the multiplier for higher Reynolds numbers. The recently reported numerical study of Lane et al.[9] also provides empirical support for a lower value of K as in Eq. 17. The correlation of Bakker and van den Akker[5] and Eq. 17 (both based on volume-averaged properties) was evaluated for estimating effective drag coefficients for gas–liquid flow in a stirred vessel by comparing simulated results with the experimental data of Bombac et al.[18]

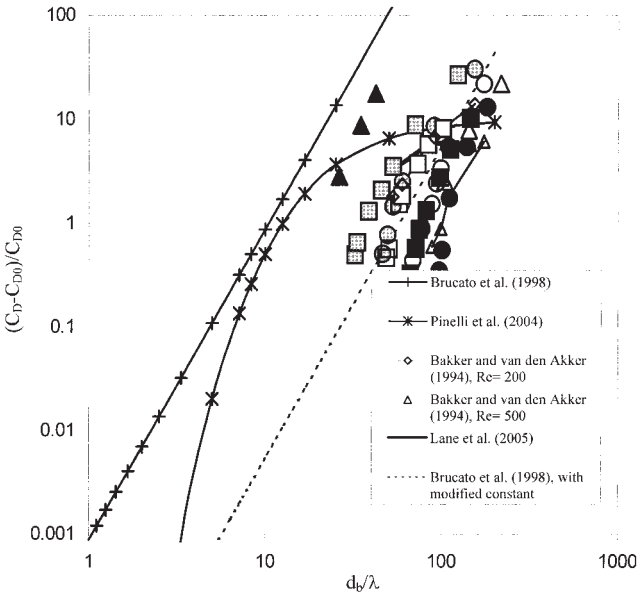

Legends:

Reynolds Number	Volume fraction 5%	Volume fraction 15%
200	□	○
500	□	○ /△*
800	■	●
50, with 500 μm solid particles	-	▲

(* data predicted from the 3-dimensional simulations)

Figure 5. Influence of turbulence, Reynolds number, and volume fraction on drag coefficient.

Gas–liquid flows in a stirred vessel

Gas–liquid flow generated by the Rushton turbine in a stirred vessel was simulated for an impeller rotational speed (N) of 266 rpm and volumetric gas flow rate (Q_g) 1.667×10^{-3} m^3/s (Fl = 0.1114; Fr = 0.3005). Before discussing the details of predicted results, the influence of grid size, the effect of interphase drag force formulation on gas holdup distribution and total gas holdup, and the influence of virtual mass were studied in detail.

Influence of grid size

As stated in the previous section, the prevailing level of turbulence influences the drag coefficient and ultimately affects the pattern of gas distribution and total gas holdup. Therefore, accurate prediction of turbulent quantities becomes essential

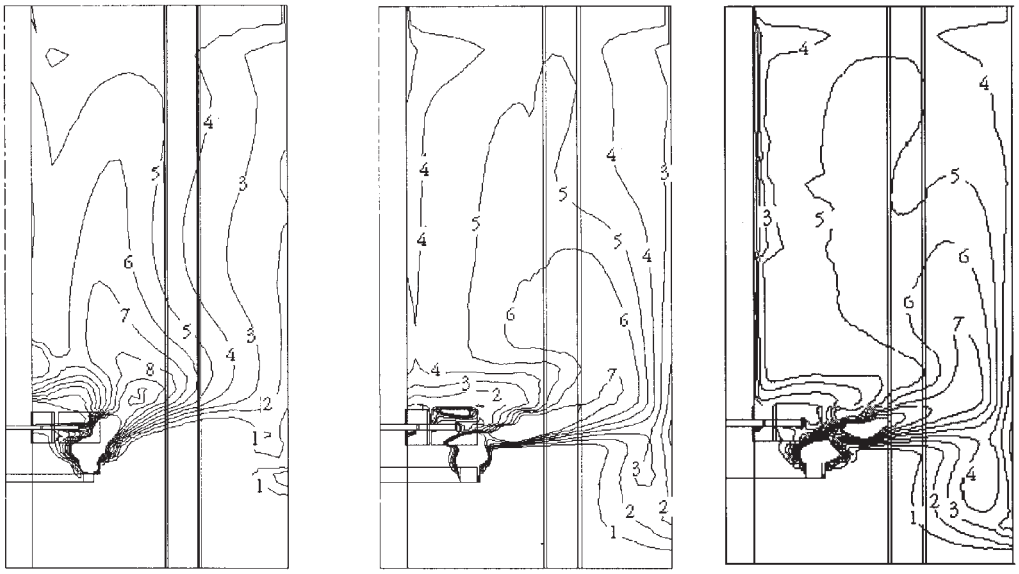

(a) Coarse grid (47,000) (b) Medium grid (240, 000) (c) Fine grid (500, 000)

(Contour labels denote the actual values of gas holdup, in percentage)

Figure 6. Influence of number of computational cells on predicted gas holdup distribution for L33 flow regime, Fl = 0.1114 and Fr = 0.3005.

(a) Coarse grid (47,000); (b) medium grid (240,000); (c) fine grid (500,000).

for correct estimation of interphase drag coefficient. The predictions of turbulent quantities are usually quite sensitive to the number of grid nodes used in the solution domain. Preliminary simulations were therefore carried out to identify the adequate number and distribution of grids. Equation 17 was used to calculate the drag coefficient. In the present work, three grid sizes—coarse grid ($r \times \theta \times z$: 25 × 44 × 43: 47 K), medium grid ($r \times \theta \times z$: 51 × 82 × 57: 238 K) and fine grid ($r \times \theta \times z$: 63 × 98 × 82: 506 K)—were considered to study the effect of grid size on predicted gas holdup distribution. The predicted gas holdup distributions for all three grid distributions are shown in Figure 6. It can be seen from Figure 6 that the predicted gas holdup distribution in the impeller discharge stream significantly changes for coarse grid (47 K) to medium grid (240 K). However, a relatively small change was observed in predicted gas holdup distribution at the impeller discharge stream for medium grid (240 K) and fine grid (500 K). Similarly, the relative change in volume-averaged energy dissipation rates when moved from medium grid to fine grid was much less (<14%) than when moved from coarse grid to medium grid (~60%). Overall, it can be said that the fine grid (~500 K grids) used in the present work adequately captures the key features of flow generated in stirred vessels. All subsequent simulations were thus carried out with the fine grid ($r \times \theta \times z$: 63 × 98 × 82).

Influence of interphase drag force

Adequate prediction of slip velocity is a key issue in simulating gas distribution and flow regimes in stirred vessels. It should be noted that distribution of key turbulence characteristics is extremely nonhomogeneous in stirred vessels. The use of local values in Eqs. 12 and 17 resulted in an unrealistically higher accumulation of gas in the lower circulation loop (arising from the significant overprediction in the values of bubble drag coefficient in the impeller discharge stream). This is not surprising, given that volume-averaged quantities were used while developing the correlations. Therefore, the use of zone-averaged values and volume-averaged values of turbulent viscosity and energy dissipation rates was examined. A comparison of the predicted gas holdup distributions of the considered cases with the experimental data (not shown here for brevity) showed that the drag coefficient estimated using volume-averaged values of Kolmogorov scale and turbulent viscosity resulted in better agreement with the experimental data. Therefore, the predicted results obtained with the volume-averaged values of key turbulence characteristics were used in the subsequent simulations.

The quantitative comparison of the predicted results and the experimental data of Bombac et al.[18] is shown in Figure 7. It can be seen from Figures 7a and 7b that the gas holdup distribution predicted based on Eq. 12 shows a gas distribution that is appreciably different from the experimental data (shown in Figure 7a). The major disagreement was observed in the region below the impeller. The impeller-generated flow was not sufficient to circulate gas in a lower circulation loop. The computational model underpredicted the total gas holdup (predicted holdup was 2.55% compared to the experimental measurement of 3.3%). This is possibly explained by underprediction of the increase in the bubble drag coefficient with using volume-averaged turbulent viscosity. A close look at Figure 5

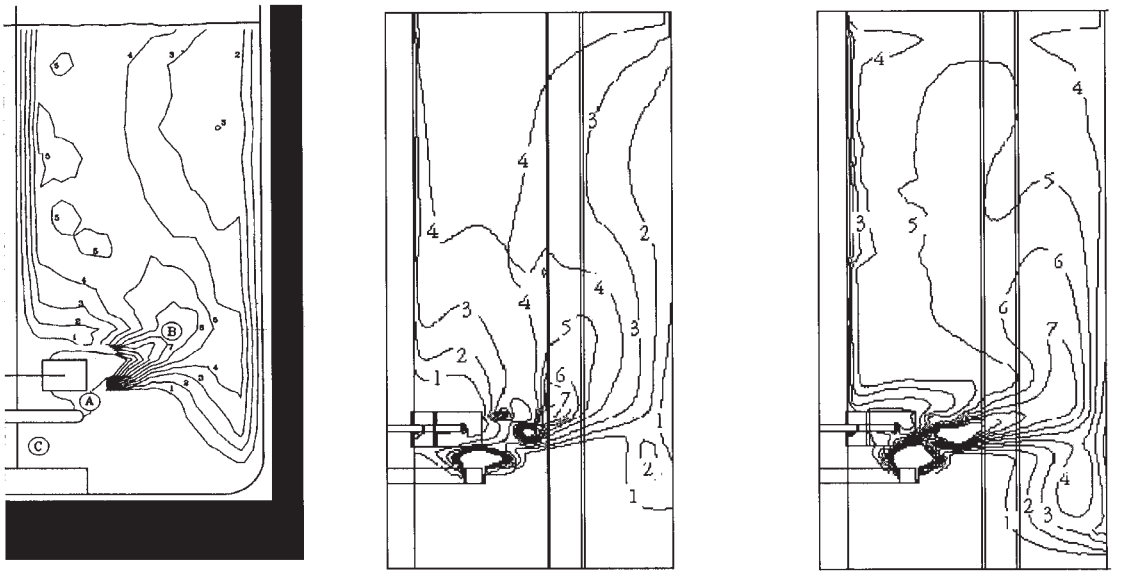

(a) Experimental (Bombac *et al.*, 1997)

(b) Predicted results with Bakker and van den Akker correlation, (Equation 12)

(c) Predicted results with modified Brucato *et al.* correlation, (Equation 17)

(Contour labels denote the actual values of gas holdup, in percentage)

Figure 7. Comparison of experimental and predicted gas holdup distribution at midbaffle plane for L33 flow regime, Fl = 0.1114 and Fr = 0.3005.

(a) Experimental[18]; (b) predicted: using Bakker and van den Akker[5] correlation; (c) predicted: using Brucato et al.[16] correlation.

(compare the CFD results with those estimated by Eq. 12 for Re = 500) explains the underprediction of the fractional increase in the bubble drag coefficient using Eq. 12 with the volume-averaged value of turbulent viscosity. The predicted results based on Eq. 17 are closer to experimental data (see Figures 7a and 7c). This model resulted in overprediction of total gas holdup (predicted holdup was 3.97% compared to the experimental measurement of 3.3%). Despite the overprediction, the predicted gas holdup distribution showed better agreement with the data than predicted by Eq. 12. All subsequent simulations were therefore carried out with the turbulent correction term for interphase drag coefficient calculated using Eq. 17.

Effect of virtual mass

The virtual mass effect is significant when the secondary phase density is much smaller than the primary phase density. The effect of the virtual mass force was studied before discussing the quantitative comparison of the predicted results with experimental data for other flow regimes. The predicted gas holdup distributions obtained with and without considering virtual mass force are shown in Figure 8. It can be seen from Figure 8 that the influence of the virtual mass force on the predicted pattern of gas distribution was significant only in the impeller discharge stream. However, the influence of virtual mass force was not found to be significant in the bulk volume of the vessel. It should be noted that the value of virtual mass coefficient used in the present study (0.5) is valid for spherical bubble and may not be appropriate for wobbling bubbles. The reported value of virtual mass coefficient is somewhat higher than 0.5 (see, for example, Tomiyama[37]). However, it should be noted that the predicted results are not very sensitive to the consideration of virtual mass terms. A comparison of the predicted results obtained with values of virtual mass coefficients as 0 and 0.5 did not show any significant differences (see Figure 8). Considering this, no specific effort was made to obtain accurate value of virtual mass coefficient and for all further simulations, the virtual mass force was not considered.

Gas holdup distribution in L33, S33, and VC flow regimes

Gas–liquid flows generated by the Rushton turbine in a stirred vessel were simulated for three gas flow regimes representing L33 (Fl = 0.1114; Fr = 0.3005), S33 (Fl = 0.0788; Fr = 0.6), and VC (Fl = 0.026267; Fr = 0.6). As discussed previously, Eq. 17—based on volume-averaged dissipation rate and Kolmogorov scale—was used to calculate effective drag coefficients. Comparisons of predicted gas holdup distributions with the experimental results at the midbaffle plane are shown in Figure 7 (L33) and Figure 9 (S33 and VC). It can be seen from these figures that the predicted gas holdup distributions for L33, S33, and VC flow regimes are in reasonably good agreement with the experimental data. However, the computational model overpredicted the values of total gas holdup. The predicted value of total gas holdup (4.85%) was higher than the reported experimental value (4.2%) for the S33 flow regime. Similarly, the predicted value of total gas holdup

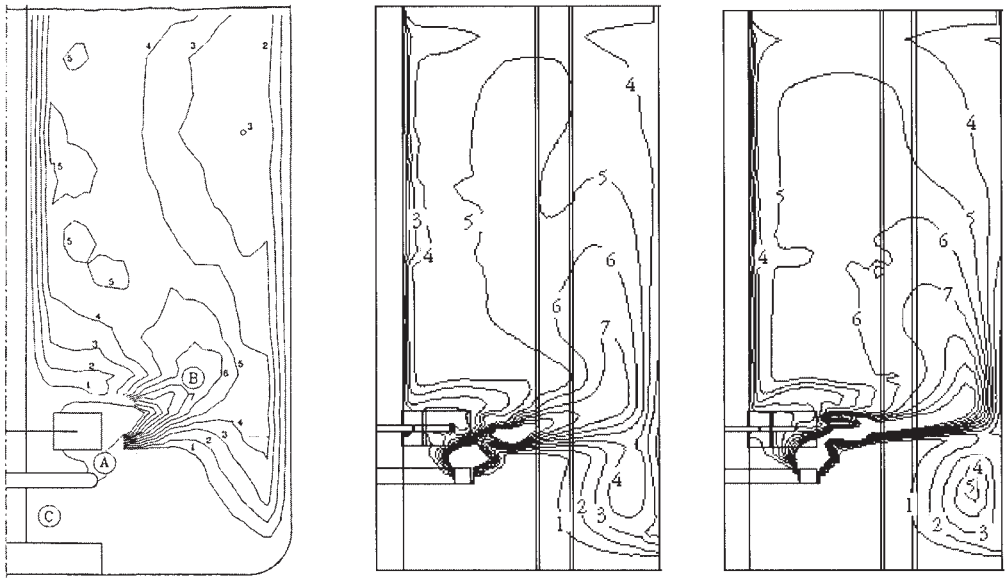

(a) Experimental: mid-baffle plane, (Bombac *et al.*, 1997)

(b) Predicted, without virtual mass effect: mid-baffle plane

(c) Predicted, with virtual mass effect: mid-baffle plane

(Contour labels denote the actual values of gas holdup, in percentage)

Figure 8. Comparison of predicted gas holdup profiles for with and without virtual mass effect for L33 flow regime, Fl = 0.1114 and Fr = 0.3005.

(a) Experimental[18]; (b) predicted, without virtual mass effect: midbaffle plane; (c) predicted, with virtual mass effect: midbaffle plane.

(2.63%) was higher than the experimental data (2.2%) for the VC flow regime.

Comparisons of axial profiles of radially averaged gas holdup for all three regimes are shown in Figure 10. It can be seen from Figure 10 that the computational model overpredicts the values of gas holdup in the region above the impeller for all three regimes. The maximum value of predicted radially averaged gas holdup occurs at an axial distance of 0.117 m for L33 and 0.107 m for S33 as well as VC regimes compared to the experimentally observed distance of 0.13 m for L33 and 0.1125 m for S33 as well as VC regimes. The predicted values of gas holdups at this maximum are underpredicted (7.3% for L33, 7.94% for S33, and 3.82 for VC) compared with the experimental value (~8.1% for L33, ~8.8% for S33, and ~4.1% for VC). Quantitative comparisons of angle-averaged values of predicted gas holdup and experimental data at three different axial locations for all three regimes are shown in Figure 11. It can be seen from Figure 11 that comparisons of the predicted values of gas holdup and experimental data are reasonably good for all three regimes. The computational model was thus able to simulate all three regimes reasonably well.

Gross characteristics

The predicted influence of gas flow rate on gross characteristics, power, and pumping numbers is also of interest. Pumping and power numbers were calculated from simulated results as

$$N_Q = \frac{2\int_{-B/2}^{B/2}\int_0^{\pi}\alpha_l r_i U_r d\theta dz}{ND_i^3} \tag{18}$$

$$N_P = \frac{2\int_V \alpha_l \rho \varepsilon dV}{\rho N^3 D_i^5} \tag{19}$$

where B is blade height, D_i is impeller diameter, N is impeller speed, r_i is impeller radius, and U_r is radial velocity. The calculated values of pumping and power numbers from the simulated results are listed in Table 2. As the gas flow rate increases, impeller pumping as well as power dissipation decreases. The extent of decrease increases with increasing gas flow rate (or, in other words, as flow regime changes from VC to S33 and further to L33). Bombac et al.[18] did not report their experimental values of power dissipation or pumping number. In the absence of such data, the predicted values were compared with the estimates of available empirical correlations.[38-40] Demonstrating the qualitatively correct trend, the CFD model reasonably predicted the decrease in power dissipation in the presence of gas compared to the estimates of these correlations. The CFD model could also correctly capture the overall gas holdup distribution and can therefore simulate different flow regimes of gas–liquid flow in stirred vessels.

Gas–liquid flow near impeller blades

It would be useful to examine the details of predicted results near impeller blades to identify the differences in flow structure of different flow regimes. Predicted flow characteristics near the impeller blades are shown in Figure 12 (isosurfaces of gas volume fraction) and Figure 13 (contours of gas volume fraction, vorticity, and turbulent kinetic energy dissipation rate) for three flow conditions.

It can be seen from Figure 12 that the computational model

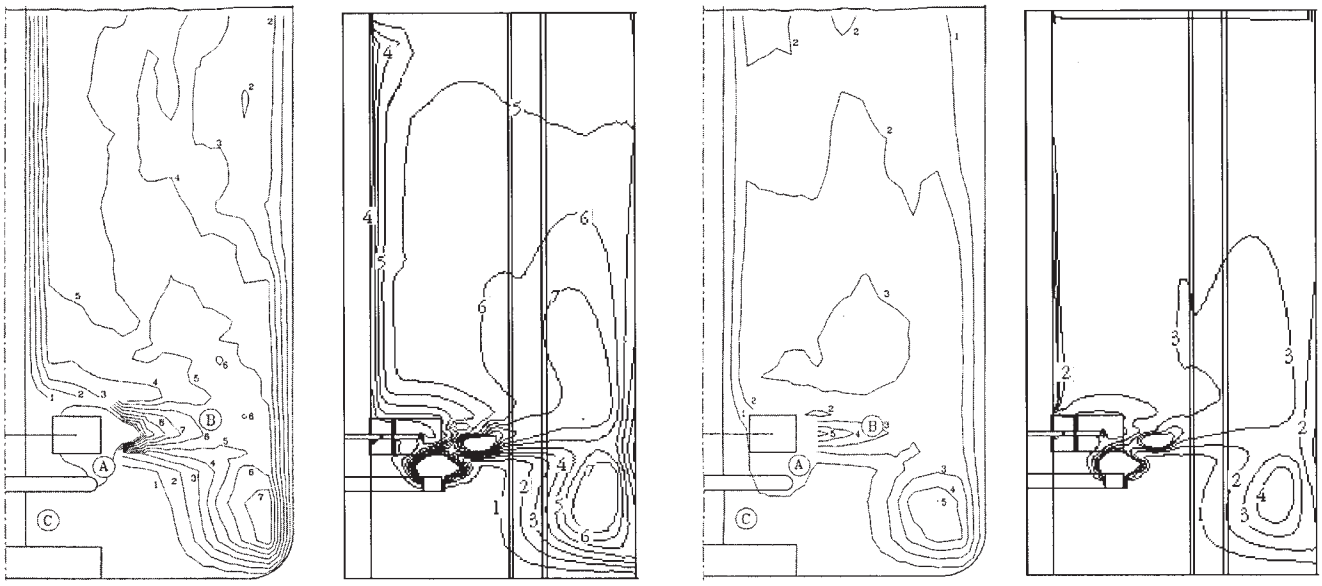

Figure 9. Comparison of experimental and predicted gas holdup distribution for S33 and VC flow regimes.

S33 flow regime, Fl = 0.0788 and Fr = 0.6: (a) Experimental[18] (midbaffle); (b) predicted (midbaffle). VC flow regime, Fl = 0.026267 and Fr = 0.6: (c) Experimental[18] (midbaffle); (d) predicted (midbaffle).

has captured the gas accumulation in the low-pressure region behind impeller blades. The sparged gas interacts with trailing vortices and is accumulated in the low-pressure region associated with the vortices. The contours and isosurface of gas volume fraction indicate that a large portion of the gas in the impeller-swept region is accumulated in the low-pressure region associated with lower trailing vortex. Examination of flow and gas accumulation around impeller blades provides clues of

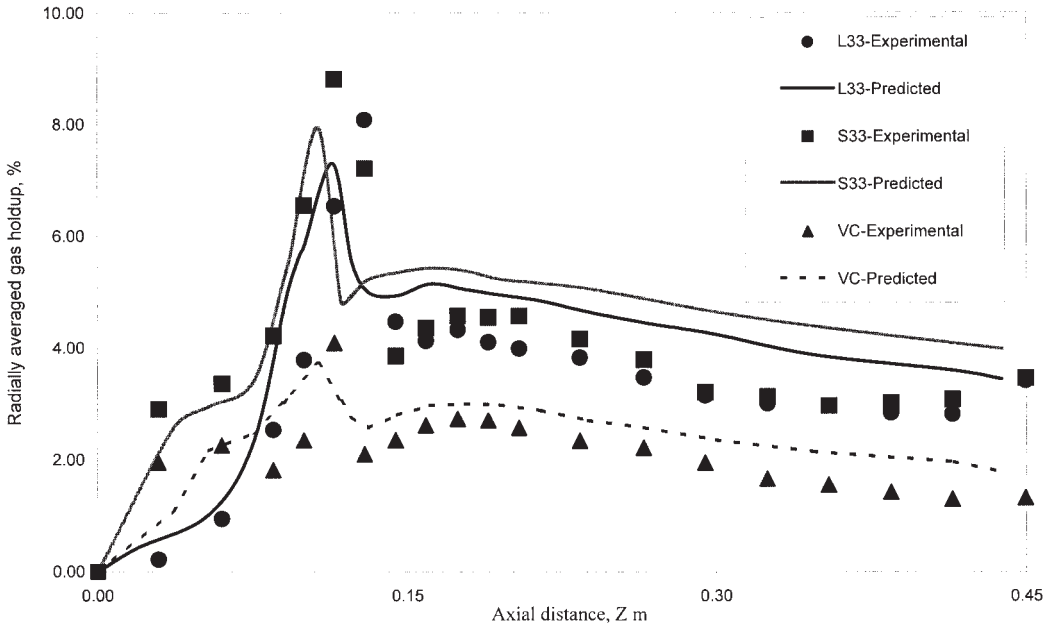

Figure 10. Comparison of predicted axial profile of radially averaged gas holdup with experimental data for L33, S33, and VC flow regimes.

Symbol denotes the experimental data of Bombac et al.[18]

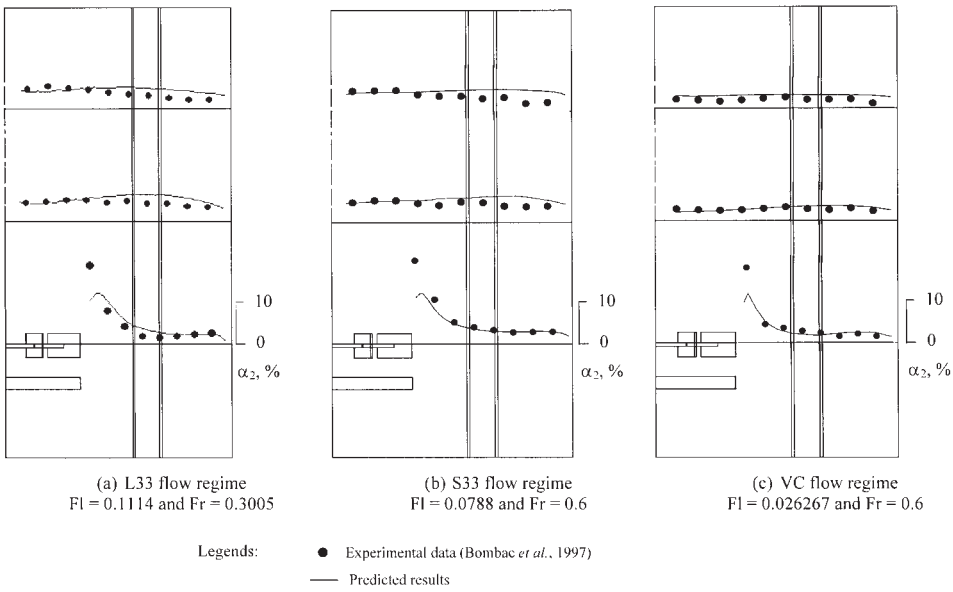

Figure 11. Comparison of predicted angle-averaged values of gas holdup (α_2) with experimental data for L33, S33, and VC flow regimes.

the prevailing flow regime. The isosurface of gas volume fraction (isovalue = 0.15) shown of the three flow regimes clearly indicates the progressive decrease in quantity of gas accumulated behind the impeller blades in the progression from the L33 regime to the VC regime by the S33 regime. The computational model did not capture the asymmetry in cavity shape for L33 and S33 flow regimes. The physical reasons for possible asymmetry in cavity shapes are not yet clear and further work is needed to capture alternating cavity structure/gas accumulation behind impeller blades. The predicted results indicate that the computational model qualitatively captures the changes in gas accumulation as the flow regime changed.

The predicted contours of vorticity and energy dissipation rate demonstrate the complex flow field within the impeller blades (Figures 13a and 13b). It can be seen that for the L33 and S33 flow regimes the sparged gas interacts with and disrupts the lower trailing vortex. High gas accumulation in the vortex core region may be the possible reason for disruption of the lower trailing vortex in L33 and S33 flow regimes. Similar behavior was not observed for the VC flow regime. The predicted contours of dissipation rate showed an increase in dissipation as the flow regime changes from L33 to VC (Figure 13b). The power dissipated within the impeller region significantly reduces with increasing gas accumulation behind the impeller blades.

Gas–liquid flow in impeller discharge stream, near vessel wall and bulk regions

The gas–liquid flow in stirred vessels is extremely complex and may exhibit different characteristics in different regions of the vessel. It should be noted that bubbles in the impeller stream would be influenced by the prevailing centrifugal forces acting in a radial direction away from the turbine blades. In the near-wall region, bubbles would interact with vorticity around baffles and exhibit characteristics different from those in other regions. The developed computational model was therefore used to examine characteristics of gas–liquid flow in the impeller discharge stream and near vessel wall.

The predicted gas holdup distribution for the L33 flow regime in the impeller discharge stream is shown in Figure 14a. The left-hand side distribution of Figure 14a is associated with

Table 2. Gross Characteristics of an Aerated Stirred Vessel

Operating Conditions	Total Gas Holdup (%)		Predicted Results		Influence of Gas on Power Number, N_{Pg}/N_P				Influence of Gas on Pumping Number, Predicted N_{Qg}/N_Q
					Predicted by CFD	Predicted by Empirical Correlations			
	Predicted	Experimental[18]	N_{Pg}	N_{Qg}		Calderbank[38]	Hughmark[39]	Cui et al.[40]	
Single-phase flow	—	—	4.15	0.66	—	—	—	—	—
VC flow regime (Fl = 0.026267; Fr = 0.6)	2.63	2.20	2.76	0.615	0.66	0.67	0.64	0.61	0.93
S33 flow regime (Fl = 0.0788; Fr = 0.6)	4.85	4.20	2.196	0.6	0.53	0.47	0.49	0.41	0.9
L33 flow regime (Fl = 0.1114; Fr = 0.3005)	3.97	3.30	1.66	0.49	0.4	0.41	0.51	0.41	0.74

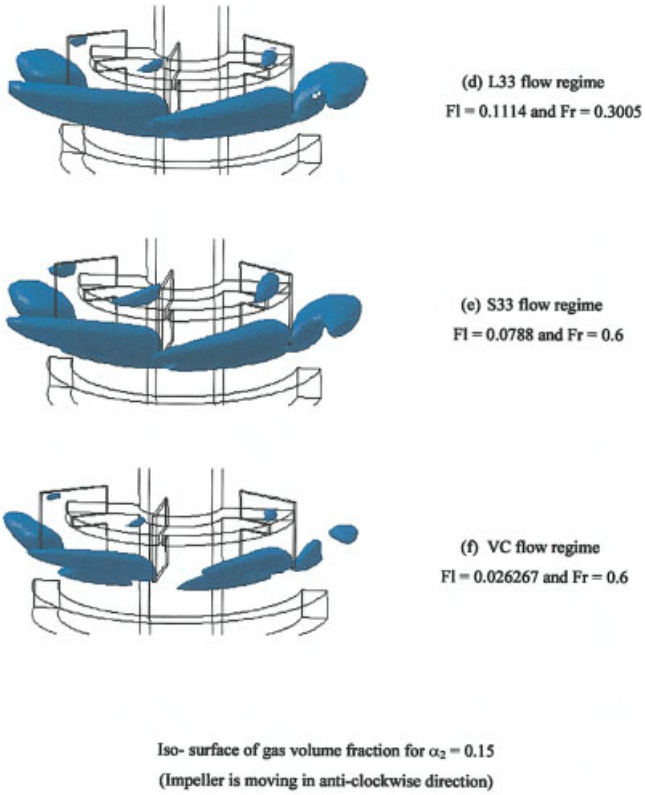

Figure 12. Predicted accumulation of gas holdup (α_2) behind impeller blades for L33, S33, and VC flow regimes.

(a) L33 flow regime, Fl = 0.1114 and Fr = 0.3005; (b) S33 flow regime, Fl = 0.0788 and Fr = 0.6; (c) VC flow regime, Fl = 0.026267 and Fr = 0.6 (isosurface of gas volume fraction: isovalue = 0.15; impeller is moving in anticlockwise direction). [Color figure can be viewed in the online issue, which is available at www.interscience.wiley.com]

the lower trailing vortex and the right-hand side distribution with the upper trailing vortex. It can be seen from Figure 14a that the computational model predicted the higher gas accumulation in the lower trailing vortices compared to the upper trailing vortices. The predicted gas holdup distribution in the impeller discharge stream shows the efficient dispersion of gas in the above impeller disc region compared to the below disc region. The predicted axial slip velocity distribution in the impeller discharge stream is shown in Figure 14b (following the same convention as that in Figure 14a). It can be seen from Figure 14b that the predicted results show the presence of negative values of the axial slip velocity in the trailing vortices. The predicted distribution of axial slip velocity in the impeller discharge stream shows almost the same values of velocities in both above- and below-disc regions. However, distinctly different variations in the slip velocity values were observed near the vessel wall in both regions. It was observed that the values of axial slip velocity increases as one approaches the vessel wall for the above-disc region, although the reduction in values of slip velocity was found in the below impeller disc region.

Similarly, distribution of the predicted values of the axial slip velocity near the vessel wall for the L33 flow regime is shown in Figure 14c. It can be seen from Figure 14c that the predicted results show an almost constant value of the axial slip velocity above and below the impeller discharge stream. However, in the impeller discharge stream, two distinct bands of slip velocity values were observed. These two bands were found to be separated at a height of the impeller disc. The upper band associated with the above-disc flow shows higher values of slip velocities compared to the slip velocity values predicted in the bulk region, whereas the values of slip velocities predicted in the lower band were found to be lower than the values observed in the bulk region. The presence of lower values of the slip velocities may be responsible for the dispersion of the

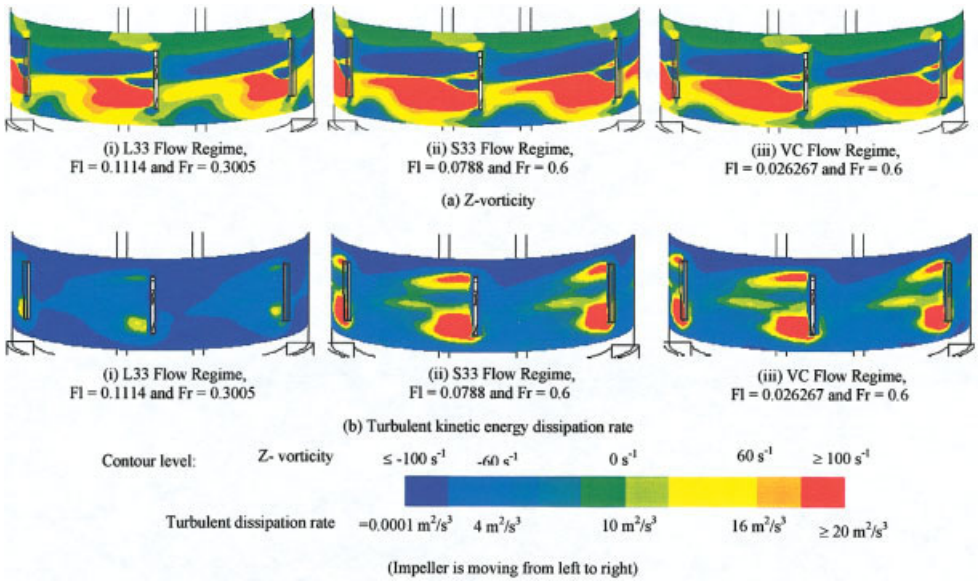

Figure 13. Details of predicted flow characteristics near impeller blades.

(a) Vorticity (z-direction, 10 uniform contours between -100 and 100 s^{-1}: (i) L33 flow regime, Fl = 0.1114 and Fr = 0.3005; (ii) S33 flow regime, Fl = 0.0788 and Fr = 0.6; (iii) VC flow regime, Fl = 0.026267 and Fr = 0.6. (b) Turbulent kinetic energy dissipation rate (10 uniform contours between 0 and 20 m^2/s^3): (i) L33 flow regime, Fl = 0.1114 and Fr = 0.3005; (ii) S33 flow regime, Fl = 0.0788 and Fr = 0.6; (iii) VC flow regime, Fl = 0.026267 and Fr = 0.6 (impeller is moving from left to right). [Color figure can be viewed in the online issue, which is available at www.interscience.wiley.com]

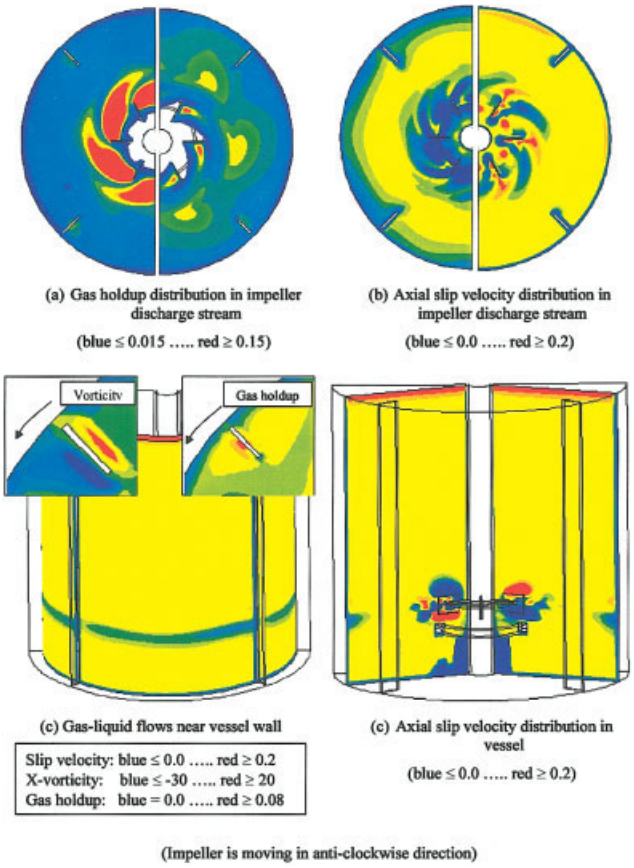

Figure 14. Details of predicted flow characteristics in impeller discharge stream and near vessel wall for L33 flow regime, Fl = 0.1114 and Fr = 0.3005.

(a) Gas holdup distribution in impeller discharge stream; (b) axial slip velocity distribution in impeller discharge stream; (c) gas–liquid flows near vessel wall; (d) axial slip velocity distribution. [Color figure can be viewed in the online issue, which is available at www.interscience.wiley.com]

gas bubbles in the lower circulation loop. The predicted results (see close-up vorticity in Figure 14c) also show the presence of two small vortices present both behind and in front of the baffles. These vortices were formed as a result of interaction of the rotating impeller discharge stream with the stationary baffles. The predicted results show a slight accumulation of the dispersed gas in these vortices (see the close-up of gas holdup distribution in Figure 14c). It was observed that the extent of gas accumulation was found to be greater in the front vortex compared to the vortex present behind the baffles.

The distributions of the axial slip velocity values at two different r–z planes are shown in the Figure 14d. The r–z planes have been selected in such a way that the left-hand side plane is located just behind the impeller blade and the right-hand side plane is just in front of the impeller blade. It can be seen from Figure 14d that the slip velocity distribution at the plane just behind the impeller blade shows the highest values of slip velocities, in both the upward and the downward directions, in the regions between sparger and impeller bottom and just above the impeller region, respectively. However, the plane just ahead of the impeller blade shows exactly the opposite distribution of the slip velocity values. The left-hand side variation of slip velocities clearly shows the tendency of the gas to interact with the trailing vortices present behind the impeller blades, whereas the slip velocity distribution at the right-hand side shows the impeller action on the gas–liquid mixture (pumping the gas–liquid dispersion in upward and downward directions). The slip velocity distributions at both planes show an almost uniform value of the slip velocity in the bulk region of the vessel.

A critical analysis of predicted results indicates that the agreement between predicted and experimental results is not very good in the impeller discharge stream. In all three cases the computational model underpredicted gas holdup in the impeller discharge stream. In the present work a single bubble diameter was used to simulate gas–liquid flow in a stirred vessel. Considering the importance of accurate prediction of slip velocity, it might be necessary to use appropriate bubble sizes. The population balance model with appropriate breakage and coalescence rates (see, for example, Buwa and Ranade[21]), which is able to simulate evolution of bubble size distribution within the vessel, may lead to better agreement with experimental data. Such a model will require an order of magnitude more computing resources. Despite some of the deficiencies, the computational model developed in this work was able to simulate observed gas holdup distribution for the three distinct flow regimes for the first time. The model was also shown to capture correct trends in accumulation of gas behind the impeller blades and reduction in power dissipation in the presence of gas. The obtained results will provide a useful basis for extending the computational models for different applications such as mixing in gas–liquid stirred reactors.

Conclusions

The preliminary simulations of gas–liquid flows in a stirred vessel highlighted the importance of correct modeling of interphase drag force. A CFD-based two-dimensional model problem was then developed to understand the influence of free stream turbulence and the presence of neighboring bubbles on the bubble drag coefficient. The two-fluid model, along with the standard k–ε model of turbulence, was then developed to simulate gas–liquid flows. The model was used to simulate gas holdup distribution in a stirred vessel operating in VC, S33, and L33 flow regimes. The predicted results were compared with the experimental data of Bombac et al.[18] The computational model was then used to examine flow structures around impeller blades for different flow regimes. The key conclusions based on this study are the following:

(1) Influence of prevailing turbulence on drag coefficient can be estimated by correlation of Bakker and van den Akker[5] and by correlation of Brucato et al.[16] with a modified ($K = 6.5 \times 10^{-6}$) constant. For both of these correlations, volume-averaged properties need to be used (turbulent viscosity for the first case and turbulent energy dissipation rate for the second case).

(2) The gas holdup distribution in a stirred vessel predicted with the modified Brucato et al.[16] correlation showed better agreement with the experimental data than other alternatives considered in this work.

(3) If the influence of turbulence on drag coefficient is appropriately accounted for, the two-fluid model can reason-

ably simulate gas holdup distribution for three different flow regimes (VC, S33, and L33). The computational model based on modified Brucato correlation overpredicted the total gas holdup values.

(4) The computational model was able to predict the influence of gas flow rate/flow regimes on gross impeller characteristics such as pumping number and power number, at least qualitatively.

(5) The model and simulations were useful to shed some light on complex flow characteristics of different regions within the vessel (impeller blades, impeller stream, and near-wall region). The model was able to capture accumulation of gas behind the impeller blades, although it was not possible to simulate formation of gas cavities behind the blades. Further work on capturing cavity formation is needed by developing a possible hybrid approach based on the VOF and the Eulerian–Eulerian approach.

Acknowledgments

One of the authors (A.R.K.) is grateful to the Council of Scientific and Industrial Research for providing a research fellowship. Department of Science and Technology Grant DST/SF/40/99 supported part of the work.

Notation

A_f = flow area, m^2
B = impeller blade height, m
C = impeller off-bottom clearance, m
C_D = drag coefficient
C_{VM} = virtual mass coefficient
d_b = bubble diameter, m
D_i = impeller diameter, m
d_{sp} = outer diameter of ring sparger, m
Eo = Eötvös number, Eo = $g(\rho_l - \rho_g)(d_b^2/\sigma_l)$
f = extra source of turbulent kinetic energy, kg s^{-3} m^{-1}
F_D = interphase drag force, N/m^3
F_{VM} = virtual mass force, N/m^3
g = acceleration arising from gravity, m/s^2
H = vessel height, m
k = turbulent kinetic energy, m^2/s^2
m = mass flow rate, kg/s
N = impeller rotational speed, rps
Fl = flow number
Fr = Froude number
N_P = power number
N_Q = pumping number
Re_b = bubble Reynolds number
P = pressure, N/m^2
Q_g = volumetric gas flow rate, m^3/s
r = radial coordinate, m
T = vessel diameter, m
t = time, s
T_L = integral timescale of turbulence, s
U = velocity, m/s
U_{slip} = slip velocity, m/s
V = volume of vessel, m^3
x = position vector, m
z = axial coordinate, m

Greek letters

α = gas volume fraction
τ = shear stress, N/m^2
τ_p = particle relaxation time, s
ε = turbulent kinetic energy dissipation rate, m^2/s^3
λ = Kolmogorov length scale, m
ρ = density, kg/m^3
μ = viscosity, kg/ms
θ = tangential coordinate

Subscripts

1 = liquid
2 = gas
q = phase number
t = turbulent

Literature Cited

1. Warmoeskerken MMCG, Smith JM. Flooding of disk turbines in gas–liquid dispersions: A new description of the phenomenon. *Chem Eng Sci.* 1985;40:2063.
2. Ranade VV. *Computational Flow Modelling for Chemical Reactor Engineering*. New York, NY: Academic Press; 2002.
3. Gosman AD, Lekakou C, Politis S, Issa RI, Looney MK. Multidimensional modelling of turbulent two-phase flows in stirred vessels. *AIChE J.* 1992;38:1947-1956.
4. Morud KE, Hjertager BH. LDA measurements and CFD modelling of gas–liquid flow in stirred vessel. *Chem Eng Sci.* 1996;51:233-249.
5. Bakker A, van den Akker HEA. A computational model for the gas–liquid flow in stirred reactors. *Trans IChemE.* 1994;72:594-606.
6. Ranade VV, van den Akker HEA. A computational snapshot of gas–liquid flow in baffled stirred reactors. *Chem Eng Sci.* 1994;49:5175-5192.
7. Ranade VV, Deshpande VR. Gas–liquid flow in stirred reactors: Trailing vortices and gas accumulation behind impeller blades. *Chem Eng Sci.* 1999;54:2305-2315.
8. Lane GL, Schwarz MP, Evans GM. CFD simulations of gas–liquid flow in a stirred tank. Proceedings of the 3rd International Symposium on Mixing in Industrial Processes, Osaka, Japan, September; 1999:21-28.
9. Lane GL, Schwarz MP, Evans GM. Modelling of the interaction between gas and liquid in stirred vessels. Proceedings of the 10th European Conference on Mixing, Delft, The Netherlands; 2000:197-204.
10. Ranade VV, Perrard M, Xureb C, Le Sauze N, Bertrand J. Influence of gas flow rate on the structure of trailing vortices of a Rushton turbine. *Chem Eng Res Des.* 2001b;79A:957-964.
11. Khopkar AR, Aubin J, Xureb C, Le Sauze N, Bertrand J, Ranade VV. Gas–liquid flow generated by a pitched blade turbine: Particle velocimetry measurements and CFD simulations. *Ind Eng Chem Res.* 2003;42:5318-5332.
12. Laakkonen M, Moilanen P, Alopaeus V, Aittamaa J. Validation of population balance models for bubbles in agitated vessel using multiblock approach. Proceedings of 5th International Symposium on Mixing in Industrial Processes, Seville, Spain; 2004.
13. Khopkar AR, Rammohan A, Ranade VV, Dudukovic MP. Gas–liquid flow generated by a Rushton turbine in stirred vessel: CARPT/CT measurements and CFD simulations. *Chem Eng Sci.* 2005;60:2215-2229.
14. Lane GL, Schwarz MP, Evans GM. Computational modelling of gas–liquid flow in mechanically stirred tanks. *Chem Eng Sci.* 2005;60:2203-2214.
15. Ranade VV, Tayaliya Y. Computational study of transfer and dissipation of impeller power. Proceedings of the Indian Society for Heat and Mass Transfer (ISHMT) 15 Conference, Pune, India; 2000.
16. Brucato A, Grisafi F, Montante G. Particle drag coefficient in turbulent fluids. *Chem Eng Sci.* 1998;45:3295-3314.
17. Pinelli D, Montante G, Magelli F. Dispersion coefficients and settling velocities of solids in slurry vessels stirred with different types of multiple impellers. *Chem Eng Sci.* 2004;59:3081-3089.
18. Bombac A, Zun I, Filipic B, Zumer M. Gas-filled cavity structure and local void fraction distribution in aerated stirred vessel. *AIChE J.* 1997;43:2921-2931.
19. Ranade VV, Karve HR, Shashi S. A computational study of gas accumulation and cavity formation behind impeller blades. Proceedings of International Conference on Multiphase Flows (ICMF), New Orleans, LA; 2001c.
20. Barigou M, Greaves M. Bubble size distribution in a mechanically agitated gas–liquid contactor. *Chem Eng Sci.* 1992;47:2009-2025.
21. Buwa VV, Ranade VV. Dynamics of gas–liquid flow in rectangular bubble columns. *Chem Eng Sci.* 2002;57:4715-4736.
22. Kataoka I, Besnard DC, Serizawa A. Basic equation of turbulence and

modelling of interfacial terms in gas–liquid two phase flows. *Chem Eng Commun.* 1992;118:221.
23. Ranade VV. Modelling of turbulent flow in a bubble column reactor. *Chem Eng Res Des.* 1997;75:14.
24. Ranade VV. Numerical simulation of dispersed gas–liquid flows. *Sadhana.* 1992;17:237-273.
25. Tsuchiya K, Furumoto A, Fan LS, Zhang J. Suspension viscosity and bubble rise velocity in liquid–solid fluidised beds. *Chem Eng Sci.* 1997;52:3053-3066.
26. Ishii M, Zuber N. Drag coefficient and relative velocity in bubbly, droplet, or particulate flows. *AIChE J.* 1979;25:843-855.
27. Clift R, Gauvin WH. Motion of entrained particles in gas streams. *Can J Chem Eng.* 1971;49:439-448.
28. Spelt PDM, Biesheuvel A. On the motion of gas bubbles in homogeneous isotropic turbulence. *J Fluid Mech.* 1997;336:221-244.
29. Clift R, Grace JR, Weber ME. *Bubbles, Drops, and Particles*. New York, NY: Academic Press; 1978.
30. Gunjal PR, Ranade VV, Chaudhari RV. Computational study of a single-phase flow in packed beds of sphere. *AIChE J.* 2005;51:365-378.
31. Ng K, Fentiman NJ, Lee KC, Yianneskis M. Assessment of sliding mesh CFD predictions and LDA measurements of the flow in a tank stirred by a Rushton impeller. *Chem Eng Res Des.* 1998;76:737-747.
32. Wechsler K, Breuer M, Durst F. Steady and unsteady computations of turbulent flows induced by a 4/45° pitched blade impeller. *J Fluids Eng.* 1999;121:318.
33. Dybbs A, Edwards RV. A new look at porous media fluid mechanics, Darcy to turbulent. In: Bear J, Carapcioglu Y, eds. *Fundamentals of Transport Phenomena in Porous Media*. The Hague, The Netherlands: Martinus Nijhoof; 1984:199-251.
34. Prakash O, Gupta SN, Mishra P. Newtonian and inelastic non-Newtonian flow across tube banks. *Ind Eng Chem Res.* 1987;26:1365-1372.
35. Uhleherr PHT, Sinclair CG. The effect of free stream turbulence on the drag coefficient of spheres. *Proceedings Chemeca'70*. Vol. 1. Melbourne, Australia: Butterworths; 1970:1-13.
36. Magelli F, Fajner D, Nocentini M, Pasquali G. Solids distribution in vessels stirred with multiple impellers. *Chem Eng Sci.* 1990;45:615-625.
37. Tomiyama A. Drag, lift, virtual mass forces acting on a single bubble. Proceedings of 3rd International Symposium on Two-Phase Modelling and Experimentation, Pisa, Italy; 2004.
38. Calderbank PH. Physical rate processes in industrial fermentation: Part I. The interfacial area in gas–liquid contacting with mechanical agitation. *Trans IChemE.* 1958;36:443.
39. Hughmark G. Power requirements and interfacial area in gas–liquid turbine agitated systems. *Ind Eng Chem Proc Des Dev.* 1980;19:641-646.
40. Cui YQ, van der Lans RGJM, Luben KChAM. Local power uptake in gas–liquid systems with single and multiple Rushton turbines. *Chem Eng Sci.* 1996;51:2631-2636.

Manuscript received Mar. 16, 2005, revision received Sep. 15, 2005, and final revision received Nov. 30, 2005.